energies

MDPI

Article

Using Numerical Analysis to Design and Optimize River Hydrokinetic Turbines' Capacity Factor to Address Seasonal Velocity Variations

Bahador Shaabani *, Vijay Chatoorgoon and Eric Louis Bibeau *

Department of Mechanical Engineering, University of Manitoba, 75 Chancellors Cir, Winnipeg, MB R3T 5V6, Canada

* Correspondence: bahadorshbni@gmail.com (B.S.); eric.bibeau@umanitoba.ca (E.L.B.)

Abstract: Seasonal velocity variations can significantly impact the total energy delivered to microgrids produced by river hydrokinetic turbines. These turbines typically use a diffuser to increase the velocity at the rotor section, adding weight and raising deployment costs. There is a need for practical solutions to improve the capacity factor of such turbines. Our solution involves using multiple turbine rotors that can be interchanged to match seasonal velocity changes, eliminating shrouds to simplify design and reduce costs. This solution requires turbines that are designed to have an easily interchanged rotor, which requires us to limit the rotor to a two-blade design to also lower costs. This approach adjusts the turbine power curve with different two-blade rotor sizes, enhancing the yearly capacity factor. BladeGen ANSYS Workbench is used to design three two-blade rotors for free stream velocities of 1.6, 2.2, and 2.8 m/s. For each turbine rotor, 3D simulation is applied to reduce aerodynamic losses and target a coefficient of performance of about 45%. Mechanical stress analyses assess the displacement and stress of the used composite materials. Numerical results show good agreement with experimental data, with rotor efficiencies ranging from 43% to 45% at a tip speed ratio of 4 and power output between 5.4 and 5.6 kW. Results show that rotor interchangeability significantly enhances the turbine capacity factor, increasing it from 52% to 92% by adapting to river seasonal velocity changes.

Keywords: renewable energy; river hydrokinetic turbine; rotor design; capacity factor; power coefficient; tip speed ratio; computational fluid dynamic; finite element analysis

check for updates

Academic Editor: Davide Astolfi

Received: 20 December 2024
Revised: 13 January 2025
Accepted: 19 January 2025
Published: 22 January 2025

Citation: Shaabani, B.; Chatoorgoon, V.; Bibeau, E.L. Using Numerical Analysis to Design and Optimize River Hydrokinetic Turbines' Capacity Factor to Address Seasonal Velocity Variations. *Energies* **2025**, *18*, 477. https://doi.org/10.3390/en18030477

Copyright: © 2025 by the authors. Licensee MDPI, Basel, Switzerland. This article is an open access article distributed under the terms and conditions of the Creative Commons Attribution (CC BY) license (https://creativecommons.org/licenses/by/4.0/).

1. Introduction

The growing demand for sustainable energy solutions has led to significant advancements in renewable technologies, including hydropower. One of the notable technologies in this field is river hydrokinetic turbines (RHKTs), which have gained attention due to their ability to utilize naturally available water velocity, which remains stable year-round [1]. RHKTs are especially beneficial for remote applications, particularly when integrated into microgrids. Additionally, deploying RHKTs in well-spaced arrays enables multiple turbines to operate collectively, generating significant energy and supplying it directly to the grid.

Kirke [2,3] highlighted that, despite the optimism surrounding the potential of hydrokinetic turbines in rivers, their deployment has been limited. Major challenges include high costs per kilowatt in real-world conditions, low capacity factors, reduced power density from slow flow velocities, and difficulties with turbine deployment and retrieval. He emphasized that for widespread adoption, turbines must be cost-effective, reliable, and adaptable to various sites. Addressing seasonal flow variations and improving capacity

factors (CFs) are crucial for ensuring consistent energy production and enhancing both economic and practical viability. Kirke [4] reiterated these challenges in 2024, noting that few companies in the RHKT industry have existed long enough to produce tangible products. For example, Smart Hydro, once deemed successful in 2020, has since ceased production, even though our team modified this turbine to successfully operate in winter conditions on the Winnipeg River. While the market for small RHKTs shows potential, there is a need for more cost-effective designs. Many companies have launched promising systems but failed to deliver practical, affordable solutions, resulting in limited turbine deployment. Their designs are often costly, bulky, and challenging to install, frequently generating less power than expected due to unrealistic flow velocity assumptions and insufficient consideration of annual variations. Our group have tested RHKTs from over 15 companies so far at the Canadian Hydrokinetic Turbine Testing Center (CHTTC) located on the Winnipeg River.

RHKTs are classified into horizontal- and vertical-axis turbines, each with its own advantages and disadvantages. Mathew and Philip [5] identified several advantages of horizontal-axis turbines, including lower cut-in speeds, a broader operational speed range, faster self-starting capabilities, and reduced torque variation compared with vertical-axis ones. Vermaak et al. [6] highlighted the benefits of horizontal-axis turbines, as well as the potential to eliminate gearboxes, thereby reducing weight and simplifying deployment. However, these turbines face challenges, including high generator coupling costs due to underwater placement and issues with floating systems caused by shroud use, which require innovative solutions. Furthermore, most hydrokinetic research has focused on large-scale technologies such as waves and ocean currents, which has slowed the development of small-scale river systems for rural areas. This focus has hindered the commercial adoption of RHKT technology, which is still in its early stages. This study focuses on addressing the disadvantages of horizontal-axis turbines while leveraging their benefits.

1.1. Capacity Factor

The CF is a key metric for evaluating a system's long-term economic performance, defined as the ratio of average power output to rated power [7]. It reflects the system's efficiency in real-world conditions, but more importantly, how well the river velocity matches the generator capacity. Most RHKT manufacturers rate turbines based on performance at approximately 3 m/s flow velocity, which is high for most rivers and can decrease significantly seasonally. Since power output scales with the cube of flow velocity, this rating can mislead expectations. For example, a turbine rated at 5 kW in a 3 m/s flow would produce only 1.5 kW in a 2 m/s flow and 0.18 kW in a 1 m/s flow [3]. Therefore, seasonal velocity variation has a strong impact on the CF. For small RHKTs, it is possible to seasonally change the rotor diameter to better match the generator size. Notably, there is no literature on rotor swamping for RHKTs to improve the CF, even though this could lead to a doubling of the CF depending on the seasonal river flow velocity variation.

1.2. Power Performance Coefficient

The power coefficient, C_p, also known as the performance coefficient, is the metric for assessing the efficiency of hydrokinetic turbines. It measures the ratio of actual power extracted by the turbine to the theoretical maximum power in the water flow, as determined by Betz's Law. In 1919, Betz [8] showed that a turbine's theoretical maximum efficiency is 59.3%; however, practical designs typically achieve lower values due to mechanical losses, wake effects, and non-ideal flow conditions. For horizontal-axis hydrokinetic turbines, C_p values generally range between 0.3 and 0.4. Guney [9] suggested that improving blade form and profile could enhance C_p. Tan et al. [10] demonstrated a two-bladed horizontal-axis turbine with a 0.585 m diameter and an efficiency of approximately 34%. Muratoglu

and Yuce [11] reported an efficiency of 43% for a three-bladed river hydrokinetic turbine. Recent advancements in blade optimization and hydrodynamic modeling have improved performance predictions. Strategies like advanced hydrodynamic shaping and adaptive control now maximize C_p in fluctuating flow environments.

1.3. Flow Velocity

Power density is highly dependent on the cube of flow velocity, making velocity a crucial factor in selecting locations and generator turbine selection. Sy and Bibeau [12] proposed a cost-effective approach for site selection and flow velocity measurement to identify optimal deployment locations using space-time image velocimetry. Turbine designs do not yet address the challenge posed by low seasonal water velocities.

1.4. Shroud

A turbine shroud enhances power output by creating a pressure gradient, effectively lowering the static pressure in the downstream area and increasing flow velocity through the turbine, allowing smaller gearless generators. Gaden and Bibeau [13] reported a 3.1-fold increase in power output with a shroud compared to a turbine alone. However, the larger diameter of the shroud introduces challenges, such as requiring greater installation depth, increased structural complexity, and higher susceptibility to clogging from debris, raising questions about its overall cost-effectiveness and operational feasibility [4]. Moreover, it does not allow rotor blade swapping.

1.5. Computational Approaches

To design an RHKT, various approaches can be employed. The blade element momentum (BEM) theory is commonly used to predict rotor performance but has limitations, including inaccuracies in cases of large induced velocities, yawed flow, and delayed stall predictions [8]. Hansen and Butterfield [14] introduced vortex wake models, which improved predictions for yawed flow and complex boundary layers. Q. Islam Md. and S. Islam A.K.M [15] demonstrated that cascade theory provides greater accuracy for high-solidity, low-tip-speed rotors. Versteeg and Malalasekera [16] highlighted significant advancements in computational fluid dynamics (CFD), noting its growing importance for designing fluid systems in aerospace, automotive, and energy industries. Despite costs, CFD's ability to shorten lead times, simulate complex scenarios, and offer detailed insights has made it indispensable. CFD offers superior accuracy in capturing complex flow dynamics, including turbulence, unsteady effects, and fluid–structure interactions, which are critical for hydrokinetic turbine design. Unlike BEM and vortex wake models, CFD can simulate the intricate behavior of the fluid flow around the rotor, especially under varying seasonal conditions and non-ideal flow scenarios. Duque et al. [17] and Serensen [18] underscored CFD's superiority in rotor analysis, with tools like ANSYS 2021 R2 CFX providing exceptional precision in simulating turbulence, unsteady effects, and fluid–structure interactions—essential for hydrokinetic turbine design.

This study demonstrates the use of CFD to design efficient RHKTs, addressing seasonal velocity variations for the first time to enhance the CF, cost-effectiveness, and ease of deployment. The approach is restricted to smaller HRKTs where the rotor can be easily pulled out and replaced with one of a different size. This study presents three key contributions:

Enhancing CF and simplifying system design: We improve RHKTs' low CF by using seasonally adjustable rotor sizes, eliminating shrouds, and incorporating two-bladed rotors to simplify near-shore deployment to lower costs. These changes reduce installation and maintenance costs, boost microgrid revenues, and simplify deployment. The elimination of the gearbox and having RHKT designs have their rotor be easily changed to adapt to seasonal velocity variations improve the economics.

Rotor design and optimization for variable velocities: The rotor design process focuses on defining and calculating the critical governing parameters of hydrokinetic systems. CFD methods are employed to analyze performance, utilizing commercial meshing tools such as TurboGrid and ICEM CFD, along with the finite volume-based solver CFX, specifically designed for turbomachinery applications. Due to high computational demands, a high-performance computer is used to perform simulations efficiently. The numerical model is validated against experimental data, concluding with an optimized turbine rotor design.

Mechanical analysis and material selection: The mechanical behavior of the rotor is analyzed using finite element analysis (FEA) with ANSYS Static Structural software 2021 R2. This approach evaluates stress and displacement across various rotor materials to ensure structural integrity under operational loads, ensuring long-term durability and reliability.

In summary, this study utilizes CFD to design an efficient two-blade RHKT, addressing challenges related to seasonal velocity variations, cost-effectiveness, and ease of deployment. Key contributions include enhancing the CF through adaptable rotor designs, optimizing rotor performance for variable flow velocities using known CFD methods, and ensuring long-term durability with mechanical analysis and material selection. By integrating these innovations, this research provides a scalable and sustainable solution for improving RHKT efficiency and reliability.

2. Materials and Methods

The following section outlines the methodologies employed in rotor design. The rotor design process follows a structured and systematic approach to ensure aerodynamic efficiency, structural integrity, and adaptability to real-world RHKT conditions. The process begins with establishing initial assumptions and calculations, which incorporate key design input parameters such as flow velocity, power output, tip speed ratio (TSR), performance coefficient and turbine radius. These parameters serve as the foundation for all subsequent design decisions. The blade geometry is then modeled using specialized CAD software (Ansys 2021 R2), BladeGen, which allows for the precise representation of the turbine's 2-blade design. This step ensures the geometry aligns with the performance goals, such as maximizing energy capture and minimizing drag. Following the geometry creation, numerical analysis is carried out to assess the performance of the rotor. This begins with preprocessing, where the computational domain is prepared, and boundary conditions and expressions are defined to simulate realistic operational conditions. An advanced turbomachinery solver, CFX, is then used to simulate fluid flow, providing insights into the aerodynamic performance of the rotor under both steady-state and transient condition. The shear stress transport (SST) model is applied in the CFD simulation. This step captures critical factors such as flow variations, wake interactions, and turbulence effects that can significantly impact rotor performance. Given the scope and objectives of this study, the SST model is sufficient to accurately simulate the key phenomena affecting hydrokinetic turbine design. Advanced turbulence models like large eddy simulation (LES) or detached eddy simulation (DES) are typically used for capturing turbulence at finer scales or in highly complex flow scenarios. However, for the current application, the SST model provides an effective balance between accuracy and computational efficiency, as it can resolve the primary flow features without the need for the additional computational cost associated with LES or DES. Once the solver has completed the simulation, the results undergo post-processing and validation to ensure the accuracy of the analysis and meet the design goals. Geometry optimization is then performed based on aerodynamic parameters to improve the design and ensure it meets performance targets.

Finally, material selection and structural analysis are conducted using FEA to assess the rotor's structural integrity under operational loads. This ensures that the rotor is not

only aerodynamically efficient but also robust and reliable for real-world conditions. The combined approach of aerodynamic and structural optimization results in a rotor design that balances performance with durability. Figure 1 presents a detailed flowchart of the design methodology, categorized into the following stages:

1. Design inputs;
2. Geometry development;
3. Numerical analysis;
   - 3.1. Preprocessing;
   - 3.2. Solver;
   - 3.3. Post-processing and validation;
4. Material selection and structural analysis.

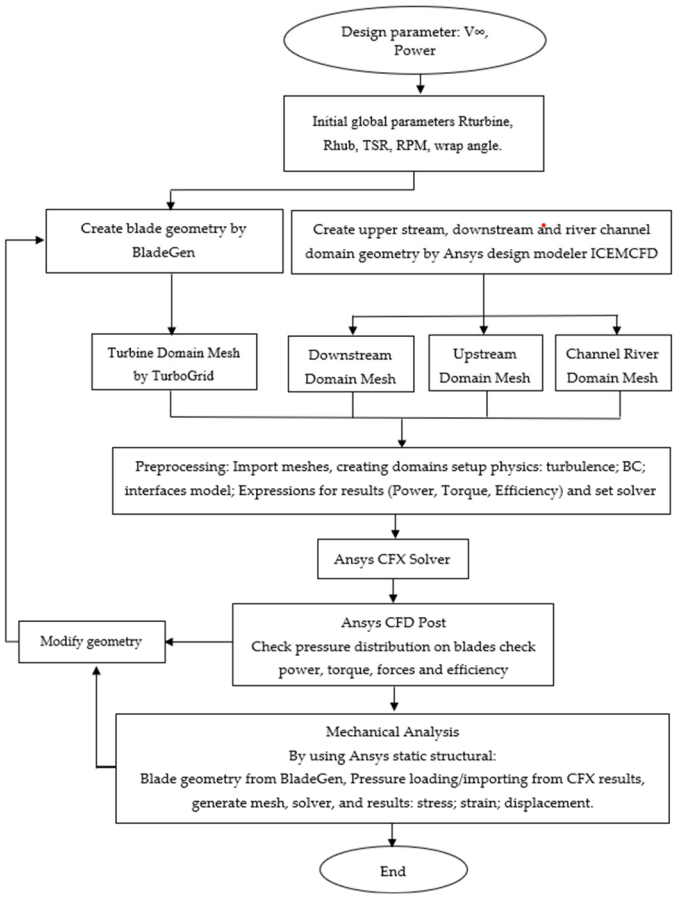


Figure 1. Rotor design methodology flowchart.

2.1. Design Inputs

The design process starts with three types of parameters: design goals, assumptions, and calculated values. Design goals include inlet velocity, $V\infty$; desired power output, P; and efficiency target, C_P. Assumptions, such as TSR; generator efficiency, η_G; and turbine mechanical efficiency, η_M, enable the calculation of the turbine radius and Beta angle, forming the basis for the turbine's geometry and further design steps.

As summarized in Table 1, the goal is to produce 5 kW of power, accounting for seasonal variations in free-stream velocities of 2.8, 2.2, and 1.6 m/s, with a target TSR of 4. The rotor design incorporates efficiency calculations, considering generator and turbine losses, with assumed efficiencies of 96% for η_G and 97% for η_M [8]. The design aims to maintain a C_p within the range of 40% to 45% [11]. The initial assumption for the hub diameter is 0.125 m for all three 2-blade rotors. This value is the initial value but is adjusted

during the optimization process based on the blade radius to achieve better performance and efficiency. The span for the tip, also referred to as the shroud radius, defines the outer boundary of the computational domain in the radial direction. The span for the tip is an important parameter in simulations, as it helps to accurately model the turbine's behavior and flow dynamics. A common practice is to apply a 2% adjustment to the turbine radius for the shroud radius. This small adjustment creates a buffer zone between the blades and the outer boundary of the computational domain, helping to prevent numerical artifacts that can arise from the boundary conditions. Additionally, the 2-blade rotor is designed to spin counterclockwise.

Table 1. Summary of design inputs.

Design Inputs	Value	Comment
Rated generator power output [kW]	5	Design goal
Generator efficiency [-]	0.96	Assumption
Turbine mechanical efficiency [-]	0.97	Assumption
Turbine hydraulic efficiency [-]	0.40	Design goal
V free stream [m/s]	2.8	Rotor 1
	2.2	Rotor 2
	1.6	Rotor 3
TSR initial [-]	4	Assumption
Rhub [m]	0.125	Rotor 1
	0.125	Rotor 2
	0.125	Rotor 2
Span for tip [-]	0.98	Blade tips needed
Blades spinning direction	Count clockwise seen from upstream	Same as for Smart Hydro
Number of blades	2	Required

The available power indicates the maximum achievable power for a specific frontal area by considering the turbine as a disc [8] and is given by the following:

$$P_{Available} = \frac{\rho}{2} C_P A V^3 \tag{1}$$

where P is the available power, ρ is the water density, C_P is the efficiency of the rotor, A is the turbine frontal area, and V is the water velocity. However, this represents the ideal power, which is not achievable according to Betz's law, but this power is used to calculate the turbine's radius as an input. During this process, losses such as η_G and η_M must be considered. Consequently, the frontal area of the actuator disc is determined as follows:

$$\frac{P}{\eta_G \eta_M} = \frac{\rho}{2} C_P A V^3 \tag{2}$$

For Rotor 1's size, the calculation for the frontal area is as follows:

$$\frac{5}{0.96 \times 0.97} = \frac{1}{2}\, 0.4 \times A \times (2.8)^3$$

$$5.37 = \frac{1}{2}\, 0.4 \times A \times (2.8)^3$$

$$A = 1.223 \text{ m}^2$$

This calculation indicates that to achieve 5 kW output power after mechanical and generator losses, a hydraulic power of 5.37 kW is required. The blade radius is calculated based on the frontal area:

$$A = \pi r^2 \text{ and } r = 0.624$$

Similarly, the radii of Rotor 2 and Rotor 3 are calculated and presented in Table 2. As mentioned earlier, the available power differs from the turbine power. The available power refers to the potential power that can be extracted from water in each frontal area. In contrast, turbine power represents the maximum power that can be harnessed by the aerodynamics of the blades. According to Betz's law, this ratio is limited to 59.3% of the available power, representing the power coefficient or efficiency of the rotor, which is calculated as follows [8]:

$$Efficiency = \frac{Turbine\ Power}{Available\ Power} \quad (3)$$

$$0.593 = \frac{P_{Turbine}}{P_{Available}}$$

Table 2. Initial design parameters.

Rotor	Velocity (m/s)	Frontal Area (m^2)	Turbine Radius (m)	Shroud Simulation Domain R (m)
1	2.8	1.223	0.624	0.634
2	2.2	2.522	0.896	0.911
3	1.6	6.555	1.445	1.469

In this study, an efficiency of at least 40% is targeted for all three rotors.

$$0.4 = \frac{5.37}{\frac{\rho}{2} C_P A V^3}$$

According to the efficiency equation, to achieve the target of 5.37 kW hydraulic turbine power with a maximum efficiency of 40% across all three rotors, the frontal area must progressively increase from Rotor 1 to Rotor 3 as the velocity decreases along the sequence. This adjustment ensures consistent power output from each rotor. As a result, according to Equation (1), the available power for all three rotors is 13.5 kW. Table 2 illustrates that the frontal area increases as the velocity decreases. Additionally, a 2% simulation domain at the tip must be considered, which shows as shroud radius.

The equation for turbine power, $P_{turbine}$, in terms of torque T and angular velocity ω, can be written as follows:

$$P_{turbine} = T \cdot \omega \quad (4)$$

where P is the power output, T is the torque applied to the rotor, and ω is the angular velocity of the rotor. Torque is directly proportional to the force exerted by the fluid on the rotor blades. This force is influenced by the pressure distribution across the blade surfaces, which depends on factors such as blade shape, angle of attack, and flow alignment. Therefore, optimizing the blade design to enhance pressure differences across the blades is critical for increasing torque. Additionally, improving blade surface area, particularly in areas where pressure gradients are significant, can enhance torque without sacrificing efficiency.

The TSR is a dimensionless number that compares the rotational speed of the rotor to the velocity of the incoming fluid. The equation for the TSR is as follows:

$$\lambda = \frac{\text{Velocity of the rotor tip}}{\text{Water flow velocity}} = \frac{\omega r}{V} \quad (5)$$

At a given TSR value, the rotor's efficiency is optimized by matching the blade's rotational speed to the fluid flow speed. Typically, the TSR is designed around an optimal value, to maximize power extraction and minimize losses. At a TSR of 4, the rotational speeds are 43, 94, and 172 rpm for Rotors 1, 2, and 3, respectively.

According to Equation (3) and as a design goal, the objective is to achieve an efficiency of at least 40%, represented as follows:

$$0.4 = \frac{T \cdot \omega}{13.5} \tag{6}$$

To maintain an efficiency of 40% or above, the torque must be improved during the optimization process while keeping a constant angular velocity for each rotor. This can be achieved by optimizing and increasing the blade surface area [8] (not the disc frontal area). Additionally, optimizing the aerodynamic parameters such as the angle of attack, blade shape, and pressure differences across the blades can lead to better performance and efficiency. Improvements to these parameters ensure better interaction with the fluid flow, maximizing the force applied to the blades and, consequently, the torque. The presence of vortices on a blade's surface can impact the pressure distribution. These vortices can produce thin zones of flow reversal and disrupt the steady flow region of separation by causing uneven pressure on the suction surface. These dynamic flow conditions can result in marked pressure fluctuations on the suction blade as the wake passes over it [19]. Optimizing the performance of a turbine requires considering the effects of vortices and pressure fluctuations.

2.2. Geometry Development

BladeGen is utilized to design a 3D model of the rotor geometry, while SolidWorks is employed to model the surrounding domains, including upstream, downstream, and the river channel. The process of creating the rotor geometry begins with the BladeGen module in ANSYS Workbench, where the blade Beta angles are defined. The blade is divided into five sections, and the optimum rotor theory is applied to determine the shape of each segment based on the radius. This process involves using the velocity triangle method to analyze the fluid's velocity components relative to the blade. Equations (7)–(10) represent the absolute velocity.

Circumferential velocity:

$$u = r\omega \tag{7}$$

Absolute velocity:

$$V_{abs} = \sqrt{{C_u}^2 + {C_m}^2} \tag{8}$$

$$C_u = \frac{2 \times g \times Head}{u} \tag{9}$$

$$C_m = v \times effective\ vel. \tag{10}$$

where r is the radius of the section; ω is the angular velocity, which is 43, 94, and 172 rpm for Rotors 1, 2, and 3, respectively; V is the water velocity; and the effective velocity is the efficiency of the water velocity, which varies under the surface. The effective velocity is 80% of the actual water velocity. Effective velocity refers to the velocity of the water that contributes to the mechanical work in a system such as a hydro turbine. While the actual water velocity can be measured at the surface, the effective velocity is typically lower due to various factors, such as the behavior of the water as it moves through the system or interacts with surfaces.

Using the absolute velocity, the leading and trailing edge blade angles are calculated using Equations (11) and (12). The calculated values for the three rotors are presented in Table 3.

Table 3. Blade span airfoil distribution and Beta angle.

Rotor	Section	r (m)	u (m/s)	C_m (m/s)	C_u (m/s)	Beta_LE (Deg)	Beta_TE (Deg)
Rotor 1	1	0.125	2.25	2.24	0.87	31.65	45.15
	2	0.252	4.54	2.24	0.43	61.43	63.76
	3	0.380	6.84	2.24	0.29	71.12	71.86
	4	0.507	9.13	2.24	0.21	75.90	76.21
	5	0.634	11.42	2.24	0.17	78.74	78.91
Rotor 2	1	0.180	1.77	1.76	1.11	20.72	45.19
	2	0.363	3.57	1.76	0.55	59.77	63.76
	3	0.545	5.37	1.76	0.37	70.62	71.85
	4	0.728	7.17	1.76	0.27	75.68	76.20
	5	0.911	8.96	1.76	0.22	78.62	78.89
Rotor 3	1	0.250	1.13	1.28	1.74	154.32	41.33
	2	0.555	2.50	1.28	0.78	53.25	62.87
	3	0.860	3.87	1.28	0.51	69.17	71.70
	4	1.165	5.24	1.28	0.37	75.27	76.28
	5	1.469	6.62	1.28	0.30	78.55	79.05

Leading edge angle:

$$\beta_{LE} = 90 - \tan^{-1} \frac{C_m}{u - C_u} \times \frac{180}{\pi} \tag{11}$$

Trailing edge angle:

$$\beta_{TE} = 90 - \tan^{-1} \frac{C_m}{u} \times \frac{180}{\pi} \tag{12}$$

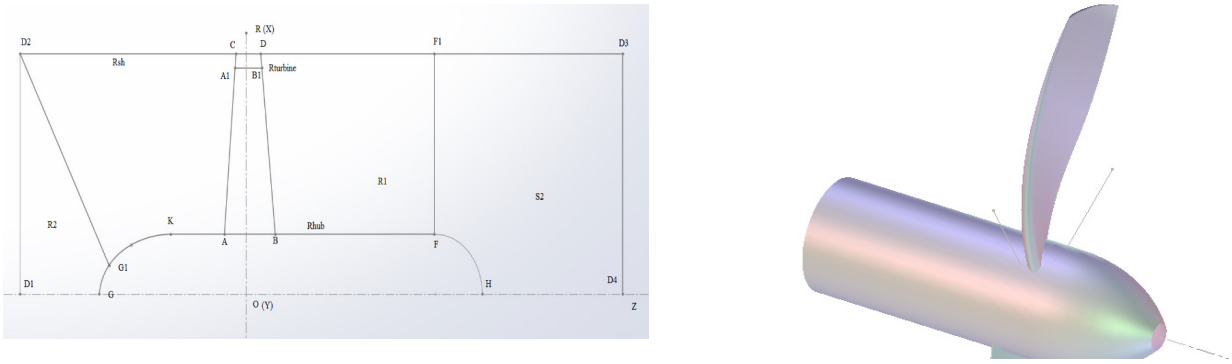
In this study, the number of sections used in BladeGen does not affect the accuracy of the CFD results. In the BEM method, forces and torques are calculated at discrete sections based on local flow conditions, and the accuracy depends on the number of sections used to approximate the overall blade performance. In contrast, CFD simulates the entire blade geometry and resolves flow interactions based on mesh quality and fluid dynamics equations. The sections in BladeGen are primarily used to define the blade's shape and design intent, while the mesh resolution and turbulence models play a critical role in determining CFD accuracy.

Unlike wind turbines, RHKTs do not have a standardized airfoil topology due to the highly site-specific nature of their design, influenced by factors such as flow velocity and depth. In ANSYS BladeGen 2021 R2, the blade Beta angle is a key parameter that dynamically adjusts the blade geometry, including the chord length and thickness, to meet the specified aerodynamic and hydrodynamic design requirements. This functionality allows for efficient customization of the blade profile to suit varying flow conditions. To initiate the design process in BladeGen, preliminary calculations using the velocity triangle method are performed to approximate the first and last points of each layer, ensuring the

desired aerodynamic performance. These initial values, as presented in Table 3, serve as the starting point but are not optimized.

During the optimization phase, the design is refined using 50 points distributed across five layers, with 10 points per layer. Each point within a layer is iteratively adjusted throughout the optimization process. This phase involves over 700 iterations of geometry regeneration and CFD simulations, ultimately resulting in an optimized blade design with improved performance and efficiency.

Figure 2 illustrates the rotor geometry created in BladeGen Ansys Workbench, showcasing the rotor configuration.



(**a**) (**b**)

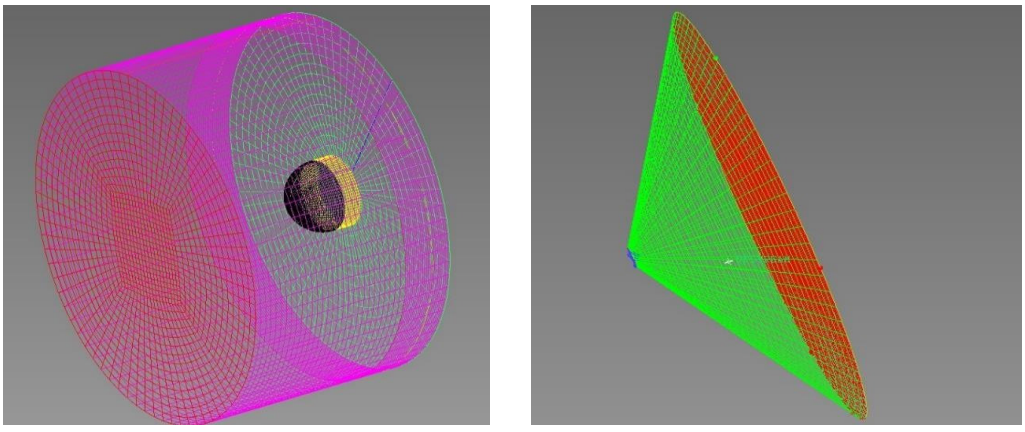
Figure 2. Geometry in BladeGen Ansys Workbench: (**a**) 2D and (**b**) 3D.

2.3. Numerical Analysis and Blade Optimization

The numerical analysis consists of preprocessing, solving, and postprocessing [16].

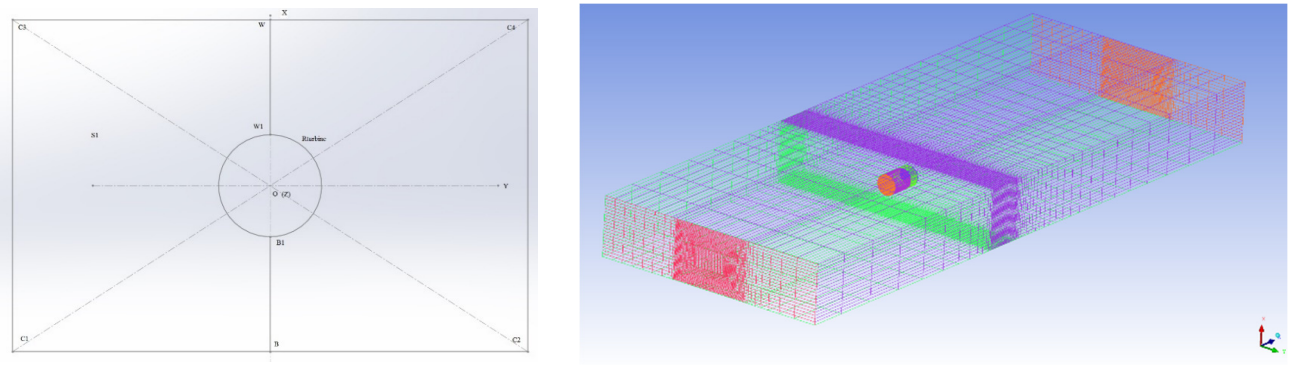
2.3.1. Preprocessing

The TurboGrid mesh generator in ANSYS Workbench is used to create a high-quality hexahedral grid for the rotors, ensuring a precise meshing pattern applied to the rotor surface. The ICEM CFD module in ANSYS Workbench is utilized to model the geometries and grids of these domains. Specifically, we use a cone geometry for the upstream domain, a cylinder for the downstream domain, and a rectangular grid for the river channel domain. These distinct geometries are chosen to accurately represent the flow characteristics in each region, as shown in Figures 3–5.



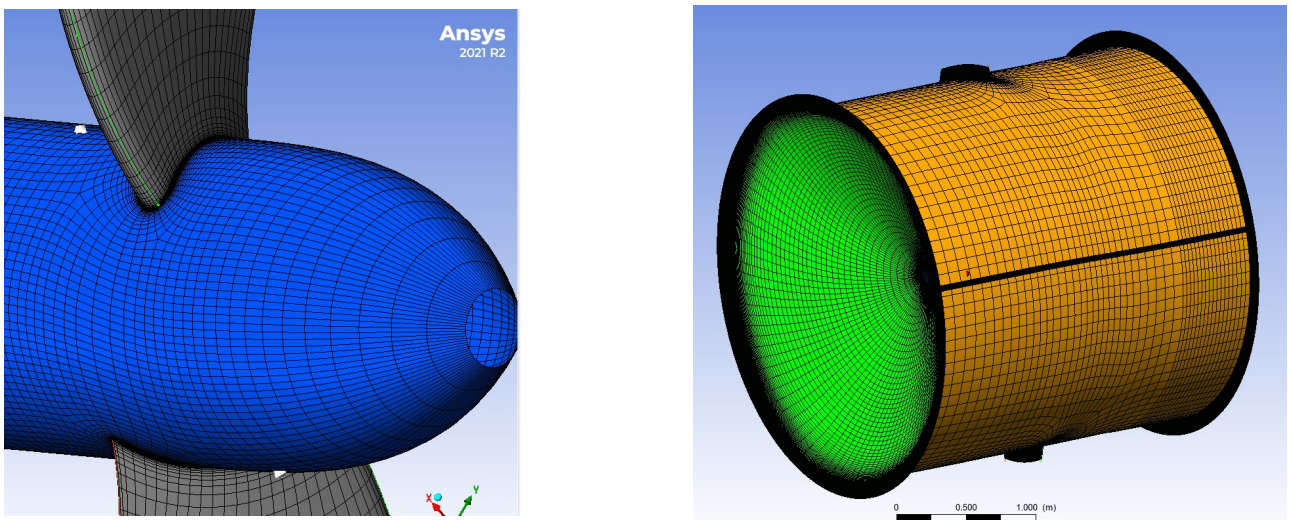
(**a**) (**b**)

Figure 3. Domain mesh: (**a**) downstream and (**b**) upstream.



(**a**) (**b**)

Figure 4. Domain mesh: (**a**) river channel cross-sectional area and (**b**) 3D view of river channel.



(**a**) (**b**)

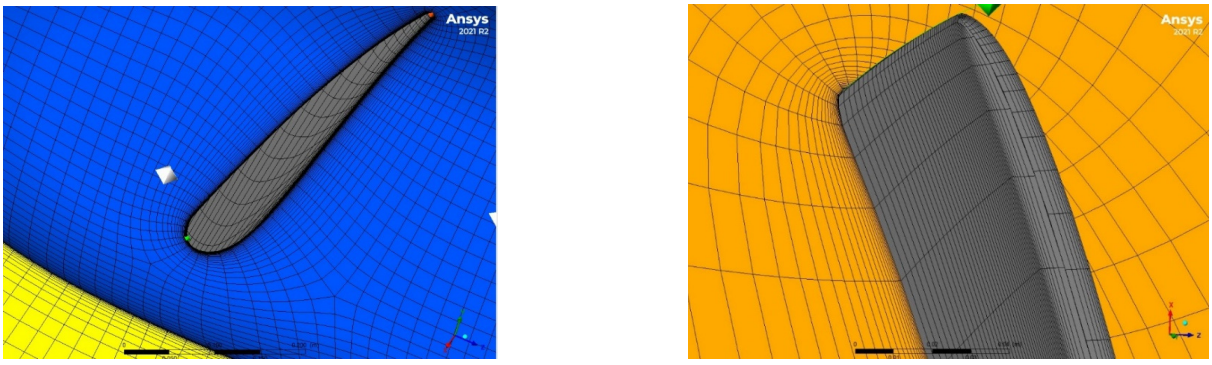
Figure 5. Mesh distribution on rotor: (**a**) rotor surface and (**b**) rotor-surrounding domain mesh.

When creating the river channel box, considering the blockage ratio is crucial. The blockage ratio, which is the ratio of the rotor area to the channel area, typically falls within the range of 0.03 to 0.05. A blockage ratio of 0.03 is selected [20]. A decrease in the blockage ratio increases the volume of water in the model, leading to more accurate simulation results. As depicted in Figure 4a, the sectional area, width, and depth of the river channel are calculated based on the size and configuration of the rotors. These values are presented in Table 4, providing a clear understanding of the channel dimensions in relation to the rotor design.

As shown in Figure 5, a high-quality hexahedral mesh is created around the rotor, with a growth rate of 1.2. The first cell height of y^+~1.7 is applied to all surfaces, intentionally positioning the first cell within the viscous sublayer ($y^+ < 5$) to meet the specifications of the SST turbulence model. The inflation layer meshing is shown in Figure 6. A grid independence study is conducted by adjusting the cell size in the inlet, outlet, and rotor domains. The properties of the considered meshes are detailed in Table 5. Each mesh is evaluated with an inlet velocity and a time step of 1.0×10^{-4} s. To ensure grid independence without compromising computational efficiency, the eight meshes are compared in terms of their results and computational cost. Mesh 5 demonstrates the fewest nodes, highest efficiency, and most reasonable iterations. Although Meshes 7 and 8 have fewer elements than Mesh 5, they exhibit higher residual values, which is not ideal, indicating that Mesh 5 provides a more accurate and reliable solution.

Table 4. River channel domain mesh dimensions.

Parameters	Rotor 1	Rotor 2	Rotor 3
Blockage ratio	0.03	0.03	0.03
distance turbine tip—water surface w1-w (m)	1	1	1
Distance tip to river bottom B1-B (m)	1	1	1
River/channel sectional area (m^2)	40.77	84.05	218.51
Channel depth C1-C3 (m)	3.2480	3.7920	4.8900
Channel width C1-C2 (m)	12.5526	22.1660	44.6842



(**a**) (**b**)

Figure 6. Inflation mesh rate: (**a**) on hub around the blade and (**b**) on rotor-surrounding near the wall.

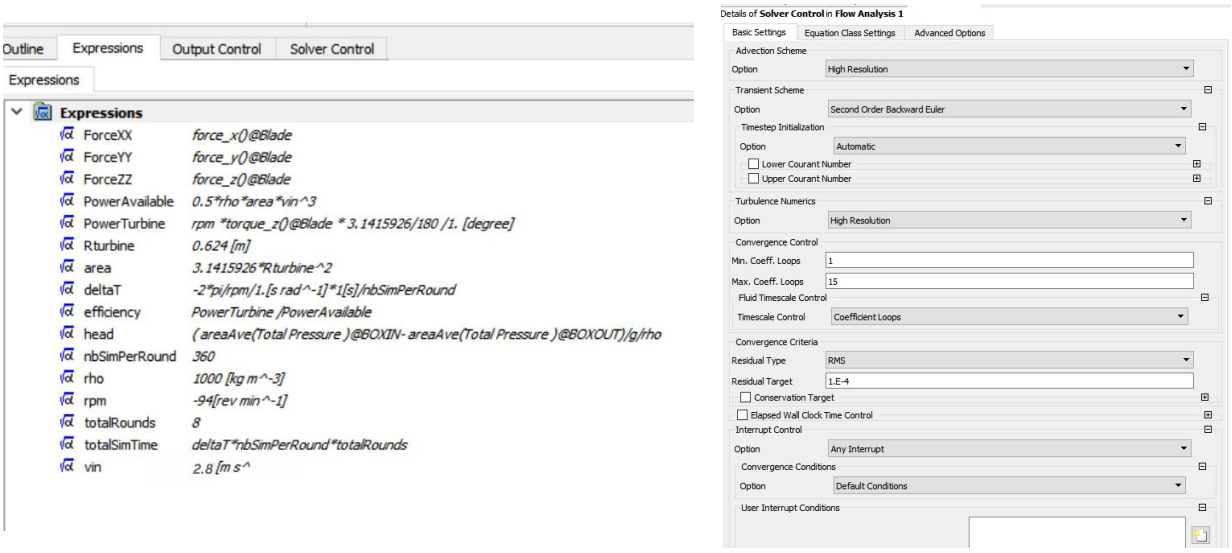
Table 5. Characteristics of meshes assessed in the grid independence study.

Section	Time Step Size (s)	Mesh Size	Number of Iterations	Number of Nodes	Efficiency %
Mesh 1	1.0×10^{-4}	4.05–1.54	441	1,579,000	42.37
Mesh 2	1.0×10^{-4}	3.52–1.02	392	1,500,000	42.57
Mesh 3	1.0×10^{-4}	3.57–1.09	528	1,345,000	42.28
Mesh 4	1.0×10^{-4}	2.5–1.02	392	1,336,300	42.61
Mesh 5	1.0×10^{-4}	1.00–1.2	401	1,124,000	43.00
Mesh 6	1.0×10^{-4}	0.8–1.06	566	1,086,000	42.44
Mesh 7	1.0×10^{-4}	1.00–1.2	Residual value > 10^{-4}	1,087,000	41.23
Mesh 8	1.0×10^{-4}	1.00–1.2	Residual value > 10^{-4}	1,000,000	40.10

The rotor and domain mesh are imported into ANSYS CFX to simulate the turbine's performance. The model consists of four domains, with various boundary conditions applied based on the interactions between these domains. The upstream and turbine domains are configured to exhibit rotational motion, with the angular velocity specified in revolutions per minute to simulate the turbine's dynamic behavior. In contrast, the downstream and river domains are modeled as stationary to accurately represent the non-rotating flow regions.

As shown in Figure 7a, a range of expressions are defined to comprehensively analyze the turbine's performance. These include the available power, turbine power, turbine radius, efficiency, angular velocity, water density, total rotations, total simulation time, the number of simulations per rotation, and water velocity. As these expressions are

for transient simulations, they provide critical insights into the turbine's efficiency and overall functionality under varying operating conditions, which are essential for accurately capturing unsteady effects in hydrokinetic turbines. Unlike steady-state models, which assume constant operating conditions, transient models can account for the fluctuations and dynamic changes in flow, torque, and blade performance that are typical in real-world hydrokinetic environments. As depicted in Figure 7b, solver control is configured to ensure the accuracy and stability of the simulation results with a residual value of 1.0×10^{-4}. A second-order backward Euler transient scheme is employed, which is well-suited for time-dependent simulations. Each time step involves 15 iterations, striking a balance between computational efficiency and result accuracy. This robust solver configuration allows the transient behavior of the turbine to be captured effectively, ensuring the reliability of the simulation outcomes.



(**a**) (**b**)

Figure 7. CFD preprocessing: (**a**) expressions for results (transient model) and (**b**) solver control.

The SST turbulence model is employed for its ability to handle complex flows involving both rotational and stationary regions. Turbine blades are treated as smooth walls with no-slip conditions, ensuring that the velocity at the blade surfaces remains zero. This approach eliminates the influence of surface roughness, enabling more precise simulation of the turbine's interaction with the flow.

Figure 8 provides a detailed view of the mesh connections established at all domain interfaces. The differing mesh sizes, resulting from the varying levels of detail required in each domain, and the rotational motion of the turbine are managed using general grid interface connections. These connections ensure seamless data transfer between domains and maintain the integrity of the simulation.

In high-turbulence cases, like rotating gears or turbines, turbulence intensity ranges from 5% to 20%. Medium turbulence occurs in systems like large pipes or ventilation, with a range of 1% to 5%, while low turbulence is seen in air over vehicles, with an intensity under 1%. For RHKTs, a turbulence intensity of 5% represents the typical operating environment, capturing the present turbulence without overestimating its effects [21]. This choice balances accuracy with computational efficiency. For the subsonic inlet flow, boundary conditions are defined with an average freestream velocity of 1.6, 2.2, and 2.8 m/s and a turbulence intensity of 5% to reflect realistic flow conditions. At the outlet, static pressure boundary conditions are specified to balance the flow dynamics.

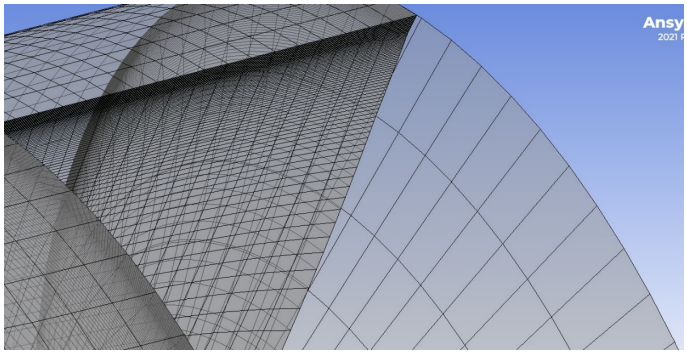


Figure 8. Mesh domains interfaces showing upstream domain and turbine domain.

2.3.2. Solver

The solver in ANSYS CFX simulates fluid flow and analyzes the aerodynamic performance of the rotor, calculating parameters such as pressure distribution, torque, and power. The SST k-ω model is employed because it is widely recognized as one of the most effective turbulence models for turbomachinery applications. Its strength lies in its ability to accurately manage both near-wall and free-stream flow conditions, making it particularly suitable for simulations performed using ANSYS CFX.

Menter [22] highlighted that while the k-ε model is less sensitive to arbitrary free-stream boundary conditions, its performance in near-wall regions, particularly for boundary layers under adverse pressure gradients, is inadequate. To overcome this limitation, Menter proposed a hybrid approach that combines the strengths of both models. This approach involves (i) transforming the k-ε model into a k-ω formulation near the wall and (ii) employing the standard k-ε model in fully turbulent regions far from the wall. The Reynolds stress computation and the k-equation align with Wilcox's original k-ω model, while the ε-equation is reformulated as an ω-equation by substituting $\varepsilon = k\omega$. Based on these insights, we selected the SST k-ω model for our simulations, as it effectively handles both the near-wall and free-stream flow regions, making it particularly suitable for turbomachinery applications.

To ensure the accuracy of the solver, we first compared the simulation results with experimental data from Stephanie Ordonez-Sanchez [23], which provided a benchmark for the power coefficient. The comparison showed that the maximum power coefficient occurred at a tip speed ratio (TSR) of 4, which fully aligned with our expectations and validated the solver's reliability. This validation, alongside prior literature, strengthens confidence in the accuracy of our simulation results and the chosen modeling approach.

2.3.3. Post-Processing

Post-processing in CFX involves analyzing and interpreting the results obtained from simulations to extract meaningful insights about the system's performance. This stage typically includes visualizing fluid flow patterns, pressure distribution, and other key variables using various tools such as contour plots, vector plots, and streamline visualizations. Additionally, post-processing allows for the calculation of performance metrics like efficiency, power output, and forces acting on surfaces, which help in understanding the behavior of the system under different conditions.

2.4. FEA Mechanical Analysis

FEA allows for the structural analysis and optimization of turbine blades. By simulating real-world conditions, FEA predicts the mechanical behavior of blades under various loads, providing valuable insights into material performance, stress distribution, and potential failure points. This allows for the development of optimized blade designs that

improve performance, durability, and safety. As the final step in rotor development, FEA is performed using the Static Structural and SpaceClaim codes of ANSYS Workbench. Prior to this, an appropriate material is chosen based on its mechanical properties.

2.4.1. Material Selection

A composite material is commonly used in turbines because of its excellent mechanical properties and light weight [24]. Integral composite materials are recommended for turbine blades due to their superior weight-to-stiffness ratio. For this study, polyether ether ketone (PEEK) carbon fibers and glass fibers are selected. Studies have shown that composites with a fiber loading of 30% to 40% demonstrate superior functionality. Additionally, incorporating nano-sized particle fillers into fiber-reinforced polymer composites can significantly enhance their overall performance [25].

2.4.2. Preprocessing

As illustrated in Figure 9, the geometry is exported from BladeGen and imported into the Static Structural module of ANSYS Workbench. To ensure accuracy in the analysis, it is crucial to apply real-world loading conditions. Therefore, the load from the CFX results is directly linked to the Static Structural module for precise analysis.

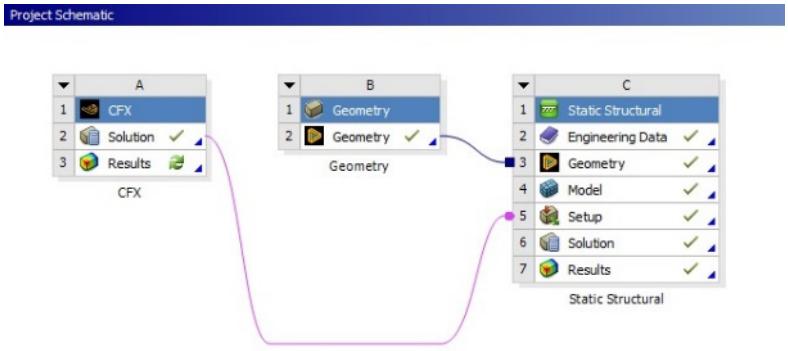
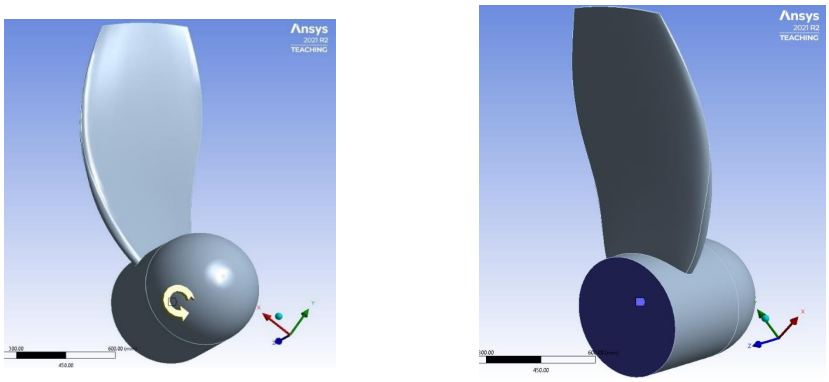


Figure 9. ANSYS Workbench setup for FEA analysis.

The boundary conditions include setting the rotational direction counterclockwise, with rotational speeds of 172 rpm, 94 rpm, and 43 rpm for Rotor 1, Rotor 2, and Rotor 3, respectively, as shown in Figure 10a. Additionally, the back hub surface is designated as a fixed surface to constrain the geometry in the Z direction, as indicated in Figure 10b.



(**a**) (**b**)

Figure 10. Boundary condition: (**a**) rotation and (**b**) fixed support.

The geometric features are modeled using a fine tetrahedral grid mesh, with the global mesh density selected to minimize discretization errors, particularly in critical failure

regions, as shown in Figure 11. The stress and displacement distributions are modeled under three different water velocities and load conditions. The maximum displacement and stress of the blade are investigated under normal steady-state conditions.

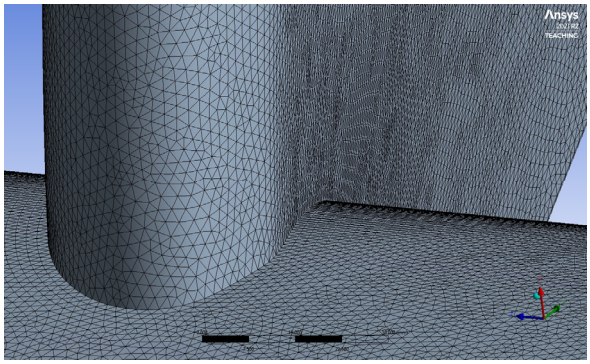


Figure 11. Rotor surface mesh.

3. Results and Discussions

This section is divided into two main parts: CFD and FEA results. The CFD results focus on evaluating the turbine's hydrodynamic performance, including parameters such as pressure distribution, efficiency, power output, and forces acting on surfaces under various flow conditions. Meanwhile, the FEA-based mechanical analysis examines the turbine's structural integrity, assessing stress distribution and displacement under operational loads.

3.1. CFD Results

The initial analysis of the three rotor configurations yielded efficiencies of 11.5%, 13.6%, and 13.3% for Rotors 1, 2, and 3, respectively. These values are typical of early-stage turbine designs, reflecting the reliance on calculation methods and simplified assumptions, such as initial blade angles and pressure distributions. Consequently, the initial rotor designs are suboptimal, which is common in the preliminary phases before optimization processes are applied. For the optimization process, the blade is divided into five sections, each with ten β angles, creating 50 points for optimization in BladeGen. The optimization process involves incrementally adjusting the value of the first point in Section 1, performing numerical analysis, and retaining the optimal value. This procedure is repeated for each subsequent point in a sequential manner. The iterative approach continues until all 50 points are optimized, leading to the identification of the optimal design parameters for the blade. Pressure differences on both the suction and pressure sides of the blades are critical for extracting maximum force. Figure 12 depicts the suction side, where the pressure is at its minimum near the leading edge and increases progressively toward the trailing edge. Conversely, Figure 13 illustrates the pressure distribution on the pressure side of the blade, showing that the maximum pressure occurs at the leading edge and gradually decreases toward the trailing edge, where it reaches its minimum. The pressure variation from the leading to the trailing edge demonstrates a vertical gradient.

Optimizing the pressure distribution led to improved rotor performance. Rotors 1, 2, and 3 were optimized using CFX solver to achieve efficiencies exceeding 40%, generating 5 kW of electricity from river water velocities of 2.8, 2.2, and 1.6 m/s, respectively. Pressure contour plots corresponding to free-stream velocities of 2.8, 2.2, and 1.6 m/s, shown in Figures 14–16, illustrate the distribution on both the suction and pressure sides of the blades. A notable pressure difference is evident along both sides of the blade, which plays a critical role in the turbine's overall performance. These optimization efforts led to improved efficiencies of 45.10%, 43.27%, and 43.42% for Rotors 1, 2, and 3, respectively.

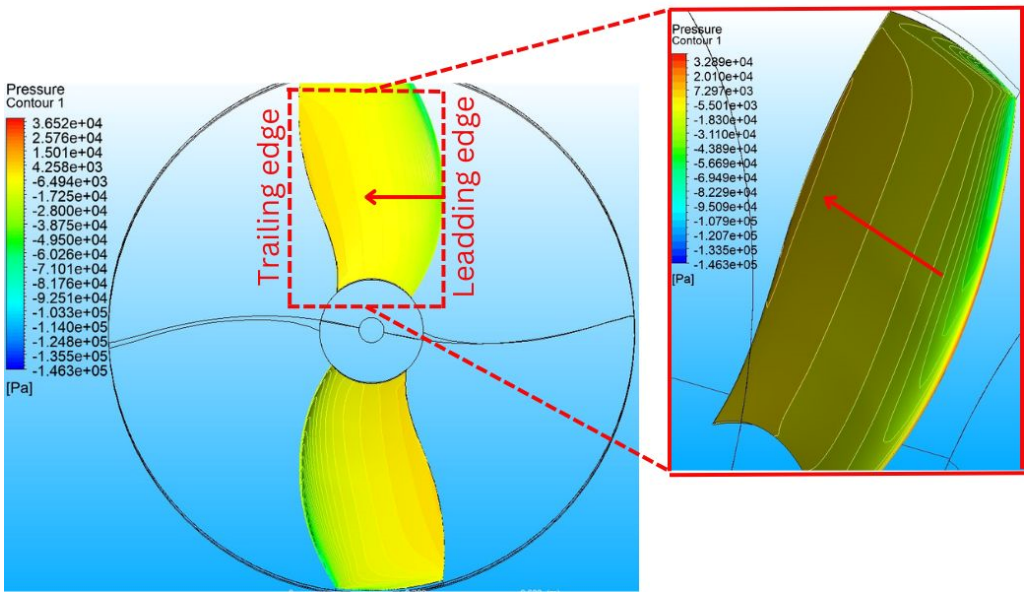


Figure 12. Pressure distribution on suction side.

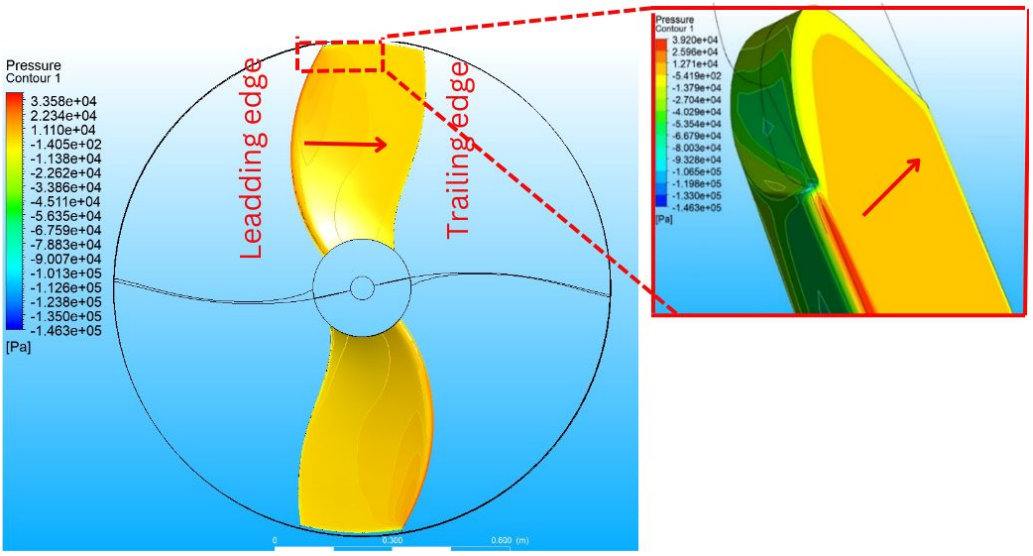
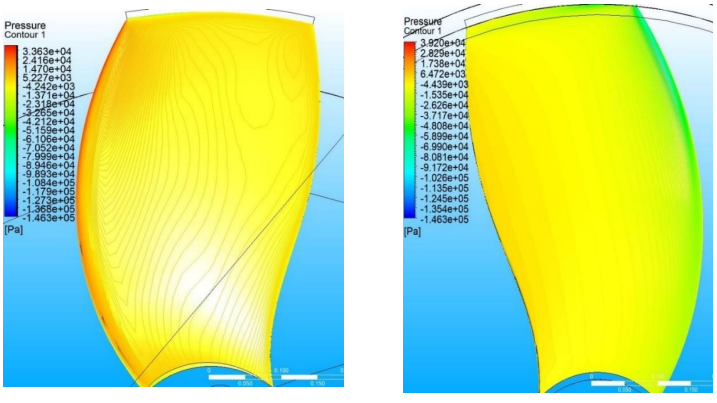
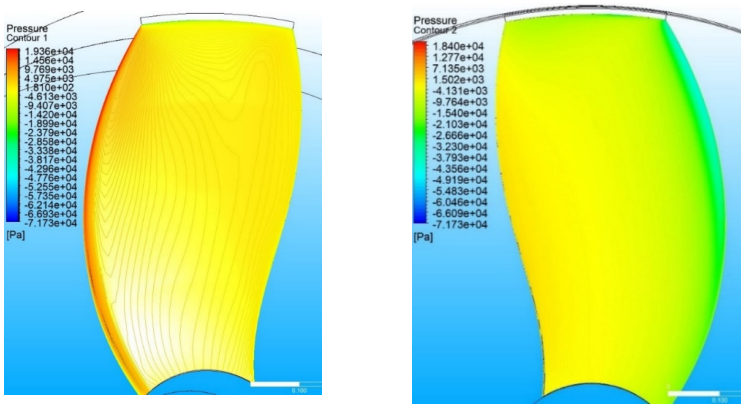


Figure 13. Pressure distribution on pressure side.



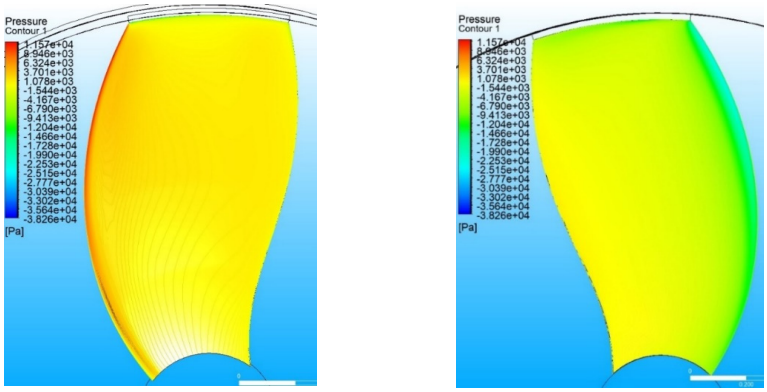
(**a**) (**b**)

Figure 14. Pressure distribution on surface of Rotor 1: (**a**) pressure side and (**b**) suction side.



(**a**) (**b**)

Figure 15. Pressure distribution on surface of Rotor 2: (**a**) pressure side and (**b**) suction side.



(**a**) (**b**)

Figure 16. Pressure distribution on surface of Rotor 3: (**a**) pressure side and (**b**) suction side.

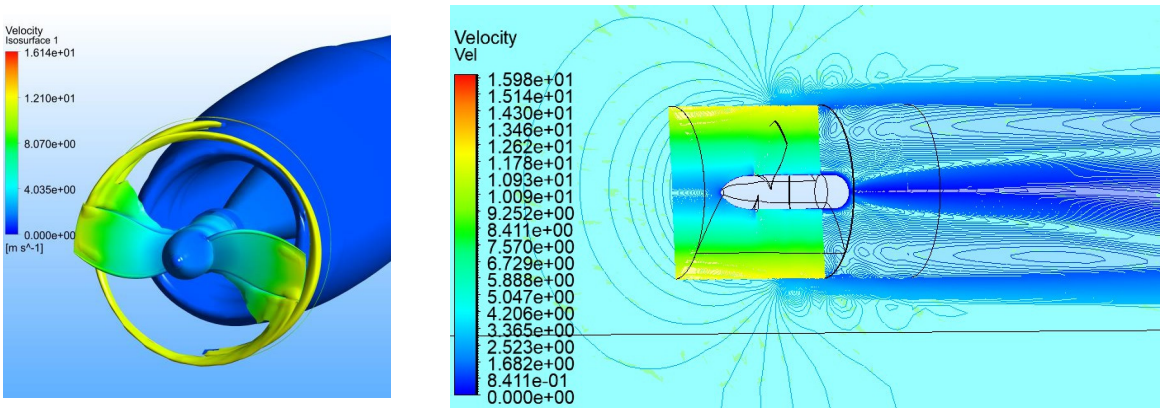
Compared to similar designs in the literature, Tan et al. [10] achieved an efficiency of approximately 34% with a two-bladed horizontal-axis turbine, while Muratoglu and Yuce [11] reported a 43% efficiency for a three-bladed river hydrokinetic turbine. The efficiencies obtained in this study are highly competitive, underscoring the potential of the proposed design to enhance hydrokinetic energy conversion efficiency.

The blade shape, fluid characteristics, and operating conditions influence the velocity distribution at the blade tip, which is crucial for turbine design optimization. As shown in Figure 17, maximum velocity occurs at the blade tip, indicating strong fluid flow in this area, which significantly impacts turbine performance.

Table 6 presents the pressure, viscous force, and torque values for the three rotors. The target output power is derived from the blade surface by applying the pressure force in the Z direction, which aligns with the flow direction. As shown in the table, the forces in the X and Y directions are nearly zero, indicating that the blades are fully optimized. The maximum pressure forces acting on the blade surfaces in the Z direction are 4.29, 5.78, and 8.17 kN for Rotors 1, 2, and 3, respectively. Compared to pressure forces, viscous forces are negligible, and drag forces are effectively zero.

Table 7 provides a detailed overview of the optimized Beta angles at both the leading and trailing edges of the turbine blades, along with their corresponding efficiency values. These data highlight the specific angles that result in maximum efficiency, offering valuable insights into the design optimization of the turbine blades. Additionally, Figure 18 depicts the variation in rotor diameters for the three rotors (Rotor 1, Rotor 2, and Rotor 3), corresponding to water velocities of 2.8 m/s, 2.2 m/s, and 1.6 m/s, respectively. These

variations reflect the design adaptations made to accommodate differing flow conditions and ensure consistent turbine performance.



(**a**) (**b**)

Figure 17. (**a**) Iso surface velocity contour and (**b**) velocity contour around rotor.

Table 6. Pressure force, viscous force, pressure torque, and viscous torque of the three investigated rotors.

Rotor	Type	X	Y	Z
Rotor 1	Pressure force (N)	0.295	−0.011	4275.20
	Viscous force (N)	0.008	−0.052	10.07
	Total force (N)	**0.304**	**−0.159**	**4285.30**
	Pressure torque (N-m)	0.037	−0.314	−362.85
	Viscous torque (N-m)	−0.003	0.007	26.97
	Total torque (N-m)	**0.037**	**−0.307**	**−335.88**
Rotor 2	Pressure force (N)	−72.235	46.309	5768.60
	Viscous force (N)	−0.356	−0.548	12.08
	Total force (N)	**−72.591**	**45.761**	**5780.70**
	Pressure torque (N-m)	−111.050	148.630	−612.42
	Viscous torque (N-m)	−0.049	0.114	48.12
	Total torque (N-m)	**−111.10**	**148.750**	**−564.29**
Rotor 3	Pressure force (N)	0.469	−0.059	8156.60
	Viscous force (N)	−0.002	0.005	17.77
	Total force (N)	**0.467**	**−0.055**	**8174.40**
	Pressure torque (N-m)	1.612	−1.931	−1351.30
	Viscous torque (N-m)	0.0002	−0.0007	111.77
	Total torque (N-m)	**1.613**	**−1.932**	**−1239.50**

Table 7. Optimum β angle of rotors and efficiency.

Rotor	Section	*r* (m)	Beta_LE (Deg)	Beta_TE (Deg)	Efficiency
Rotor 1	1	0.125	19.53	74.16	45.10%
	2	0.252	42.10	80.91	
	3	0.380	52.74	83.47	
	4	0.507	54.44	85.16	
	5	0.634	57.82	88.31	

Table 7. *Cont.*

Rotor	Section	*r* (m)	Beta_LE (Deg)	Beta_TE (Deg)	Efficiency
Rotor 2	1	0.180	22.36	77.40	43.27%
	2	0.363	44.91	83.73	
	3	0.545	54.29	85.10	
	4	0.728	55.35	86.10	
	5	0.911	57.83	88.31	
Rotor 3	1	0.25	26.37	73.80	43.42%
	2	0.555	45.92	82.26	
	3	0.860	54.44	86.19	
	4	1.165	55.54	86.26	
	5	1.469	58.19	88.67	

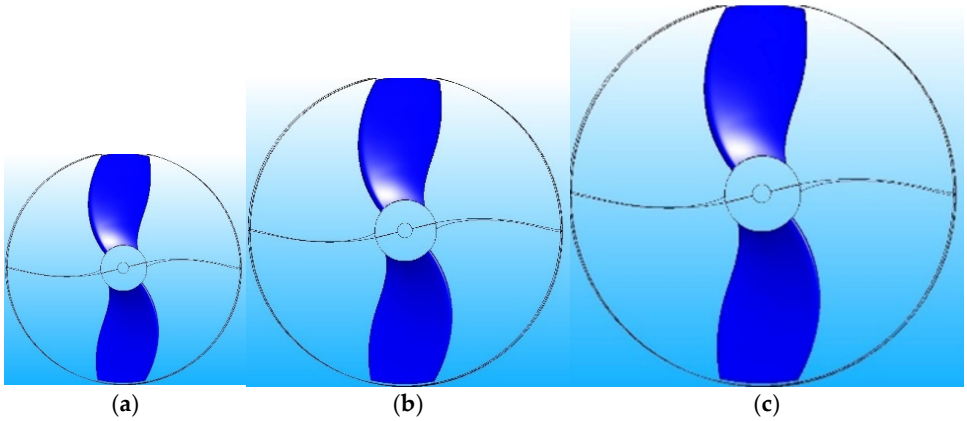


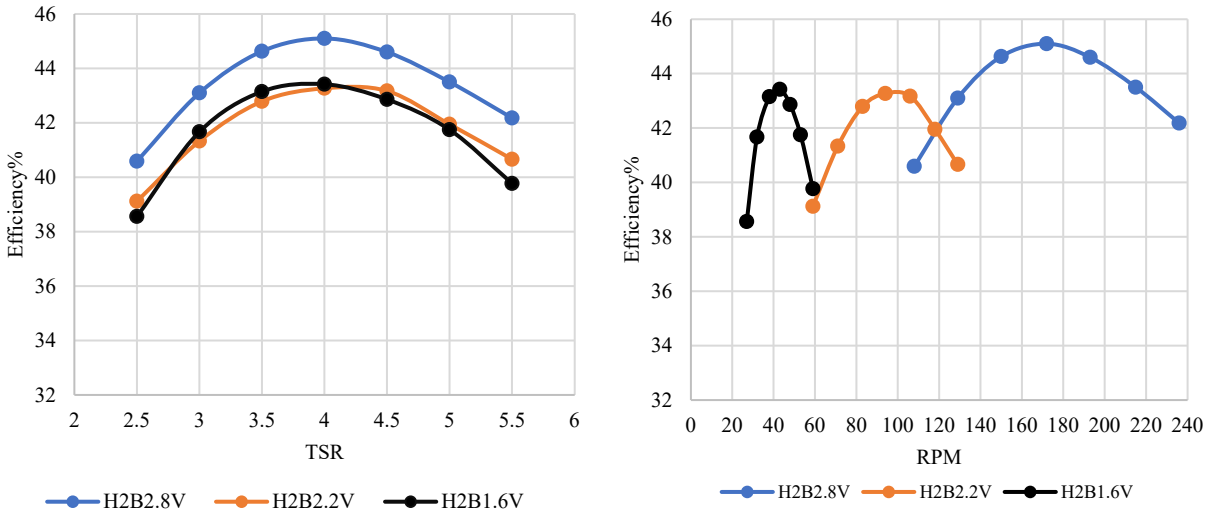
Figure 18. Rotor geometry left to right: (**a**) Rotor 1 (r = 0.624 m), (**b**) Rotor 2 (r = 0.896 m), and (**c**) Rotor 3 (r = 1.445 m).

3.1.1. Efficiency

Figure 19 presents a detailed plot of turbine efficiency as a function of TSR and rotor speed, illustrating performance trends across a wide range of operating conditions. The results indicate that maximum efficiency is achieved at a TSR of 4, corresponding to rotational speeds of 172 RPM for Rotor 1, 94 RPM for Rotor 2, and 43 RPM for Rotor 3. Notably, the data reveals that efficiencies exceeding 40% can be consistently achieved within a speed range of 32 to 236 RPM, emphasizing the turbine's adaptability to varying flow conditions. This study highlights a novel approach to harnessing hydropower by employing all three rotors throughout the year, collectively generating 5 kW of electricity with an efficiency exceeding 40%. These findings underscore the turbine's potential as a sustainable and reliable energy solution, effectively utilizing varying flow velocities to maintain high efficiency. The approach required an RHKT design whose rotor can be easily interchanged, which is facilitated by a two-blade rotor.

The CFD results are validated through a rigorous comparison between the simulation outcomes and real-world data obtained from existing case studies. To ensure the reliability and accuracy of the findings, a comparative analysis is conducted using experimental data from Stephanie Ordonez-Sanchez [23], a well-established reference in turbine performance evaluation. The simulation achieves a maximum efficiency of 43% at TSR of 3.6, as illustrated in Figure 20, closely aligning with the experimental benchmarks. This alignment not

only underscores the validity of the CFD model but also demonstrates its effectiveness in accurately replicating real-world hydrodynamic behaviors in world conditions.



(**a**) (**b**)

Figure 19. (**a**) Efficiency as a function of TSR and (**b**) efficiency as function of RPM.

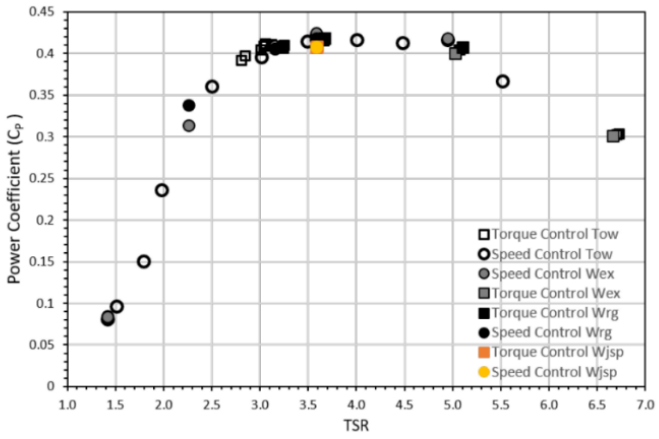


Figure 20. Experimental result extraction by Stephan Sanchez [23].

The final specifications of the rotors are presented to highlight the key design parameters and performance outcomes achieved through this study. Table 8 provides a comprehensive summary of the dimensions and results for the three rotors, each uniquely designed and optimized for specific operating conditions. The table includes critical details such as rotor diameter, blade length, hub length, TSR, angular velocity, and coefficient of performance. These specifications showcase the meticulous design process that accounted for hydrodynamic factors to achieve maximum performance. With over 70 RHKT deployments by our research group on the Winnipeg River, the use of a two-blade rotor without a shroud significantly lowers deployment and retrieval costs.

Table 8. Rotor specifications.

	Rotor 1	Rotor 2	Rotor 3
Number of blades	2	2	2
Turbine radius	0.624 m	0.896 m	1.445 m
Hub radius	0.125 m	0.180 m	0.250 m
Free stream velocity	2.8 m/s	2.2 m/s	1.6 m/s
TSR	4	4	4
RPM	172	94	43
C_p	**45.10**	**43.27**	**43.42**

3.1.2. Capacity Factor

Table 9 demonstrates that the maximum CF of 52% is achieved when a single rotor is utilized continuously throughout the year. However, this observation highlights a significant limitation of current river hydrokinetic turbines: their inability to maintain consistent energy production during periods of low water velocity. For instance, energy delivery gradually decreases from February (825.4 kWh) to January (680.1 kWh). As shown in Table 9, a significant drop is observed when comparing June (4423 kWh) with January (680.1 kWh), highlighting the sharp decline in energy production from high-velocity summer seasons to low-velocity winter periods.

Table 9. The CF of Rotor 1 using simple linear monthly velocity variation.

Month	Velocity (m/s)	Radius (m)	Area (m^2)	C_p	kW	kWh
Jan	1.5	0.6240	1.2233	0.451	0.9	680.1
Feb	1.6	0.6240	1.2233	0.451	1.1	825.4
Mar	1.8	0.6240	1.2233	0.451	1.6	1175.2
Apr	2.2	0.6240	1.2233	0.451	2.9	2145.7
May	2.2	0.6240	1.2233	0.451	2.9	2145.7
Jun	2.8	0.6240	1.2233	0.451	6.0	4423.7
					12 months	22,791.7
					Average kW	3.11
					CF	**0.52**

Figure 21 presents the yearly CF diagram for the utilization of the smallest rotor across all seasons. The diagram vividly depicts how the CF fluctuates throughout the year, corresponding to seasonal variations in water flow velocity. Notably, the performance of the rotor remains robust during high-velocity periods, resulting in a higher CF. However, a significant decline in CF is observed during low-velocity periods, particularly in winter months, when water flow rates are substantially reduced.

By utilizing three interchangeable rotors tailored to the varying seasonal flow conditions, the CF of the hydrokinetic system shows a remarkable improvement, increasing from 52% to 92%. This improvement is achieved by adapting the rotor design to the seasonal variations in water flow velocity. In particular, the use of a larger frontal area rotor during the winter months, when water velocity tends to be lower, significantly enhances energy production. As demonstrated in Table 10, the strategic increase in the frontal area of the rotor during low-flow periods effectively doubles the overall yearly CF, resulting in a more reliable and efficient energy generation system throughout the year, applying an arbitrary linear velocity variation throughout the year.

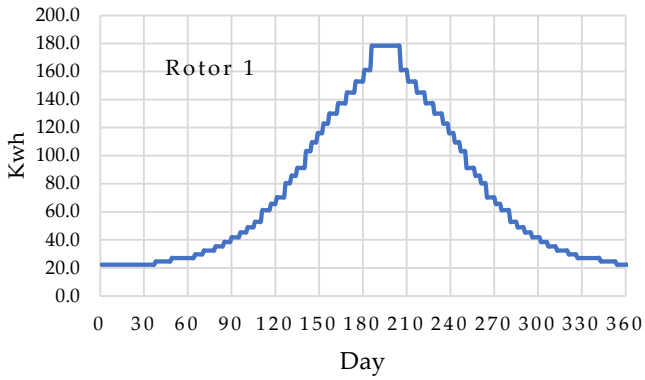


Figure 21. The yearly CF by using the smallest rotor—Rotor 1—which is typical of all installations for RHKTs and is matched to the generator size and maximum anticipated velocity.

Table 10. Simple analysis showing doubling of CF by changing rotors using simple linear variation of velocity during a year.

Month	Velocity (m/s)	Radius (m)	Area (m^2)	C_p	kW	kWh
Jan	1.5	1.4450	6.5597	0.434	4.8	3511.2
Feb	1.6	1.4450	6.5597	0.434	5.8	4261.3
Mar	2.0	0.8960	2.5221	0.432	4.4	3189.0
Apr	2.2	0.8960	2.5221	0.432	5.8	4244.6
May	2.6	0.6240	1.2233	0.451	4.8	3541.8
Jun	2.8	0.6240	1.2233	0.451	6.0	4423.7
					12 months	43,445.6
					Average kW	4.96
					CF	**0.92**

Moreover, by incorporating annual river velocity data, it becomes possible to develop a nationwide strategy for optimizing the performance of hydrokinetic turbines. These data allow for the establishment of a targeted CF tailored to regional flow conditions, enabling the more precise selection of rotor sizes and designs for various geographical locations. Such an approach ensures that turbines operate at peak efficiency throughout the year, maximizing energy production while adapting to the dynamic flow conditions of rivers across the country.

Figure 22 displays the annual CF diagram for the system using three different rotors across the year.

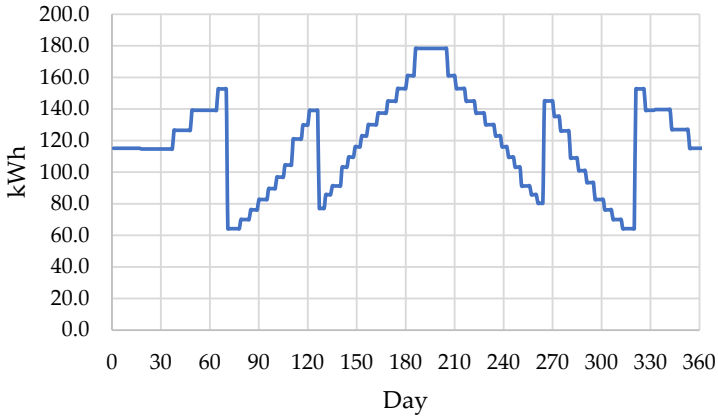
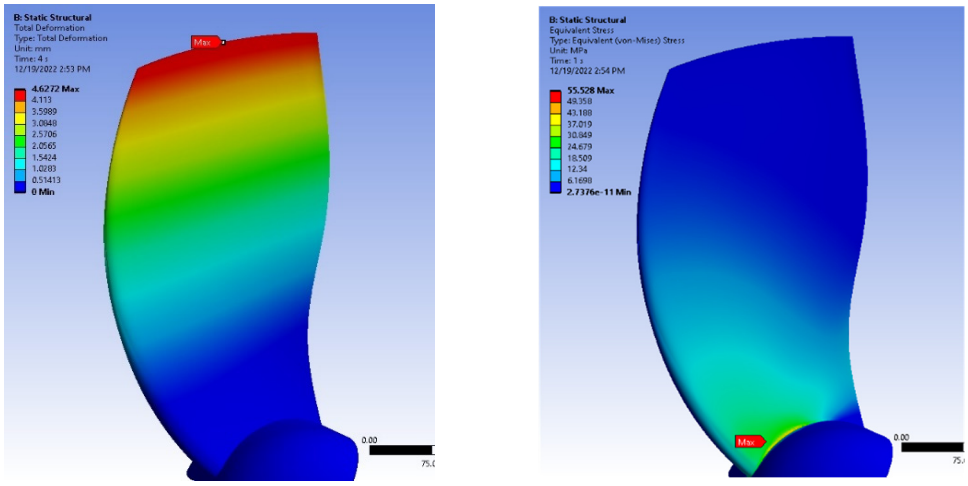


Figure 22. Yearly power production when changing the rotors seasonally increases the yearly power factor as the rotor size is more suited to the seasonal velocity.

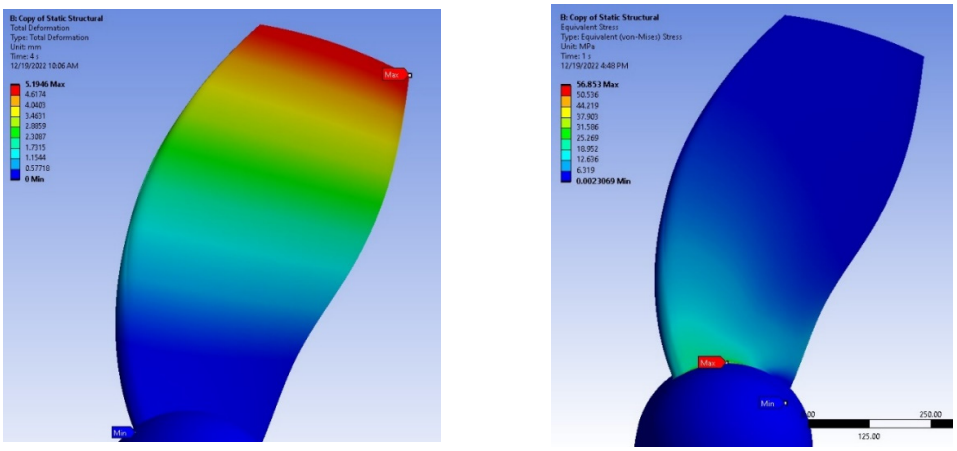
3.2. FEA Mechanical Analysis Results

Figures 23–25 provide a detailed simulation of the stress distribution and areas of maximum deformation for the rotors. As shown in these figures, the displacement gradually increases from the blade root to the tip, with minimal deformation observed up to the midpoint of the blade. This indicates that the blade's structural integrity remains largely intact in the central region, which is crucial for maintaining stability during operation. However, the maximum deformation is concentrated at the blade tip, where the aerodynamic forces are typically the strongest. Additionally, the highest stress concentrations are observed near the root area, particularly at the leading edge, where the structural load is most intense. These findings highlight critical structural considerations for rotor performance under varying load conditions. The increased blade thickness at the root is designed to handle these stresses, ensuring that the rotor can withstand high loads without compromising its structural integrity.



(**a**) (**b**)

Figure 23. Rotor 1: (**a**) maximum displacement and (**b**) maximum equivalent stress.

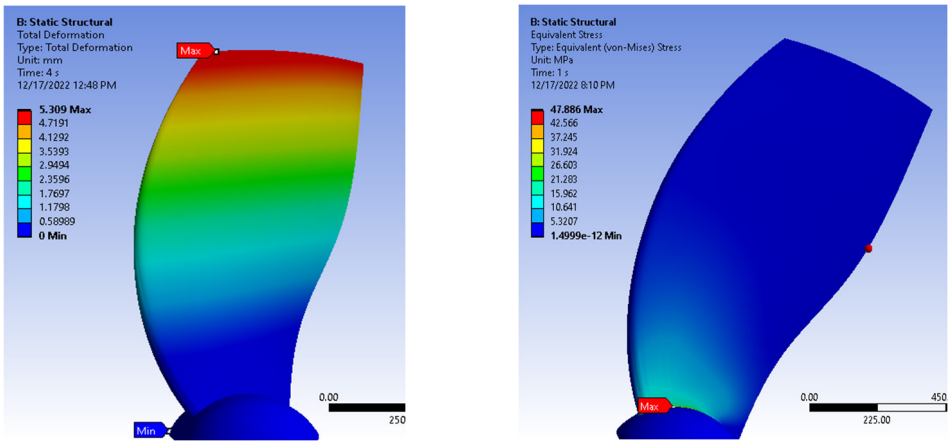


(**a**) (**b**)

Figure 24. Rotor 2: (**a**) maximum displacement and (**b**) maximum equivalent stress.

Table 11 summarizes the maximum deformation and equivalent stress for the rotors. The results show that PEEK–carbon fiber with 40% loading performs optimally under the specified load conditions compared to other materials. The displacement for stainless steel is 0.84, 0.94, and 0.97 mm for the three rotors, respectively, while the displacement for carbon fiber is slightly higher but still within acceptable limits. In terms of displacement,

stainless steel is the best option due to its lower deformation values. However, when considering the study requirements, such as weight reduction, PEEK–carbon fiber with 40% loading meets all criteria and is the preferred choice for this application.



(**a**) (**b**)

Figure 25. Rotor 3: (**a**) maximum displacement and (**b**) maximum equivalent stress.

Table 11. Maximum deformation and equivalent stress.

Rotor	Material	Maximum Deformation (mm)	Maximum Equivalent Stress (MPa)
Rotor 1	Stainless steel	0.84	52.72
	PEEK–carbon fiber 40%	4.63	55.53
	PEEK–carbon fiber 30%	6.21	55.47
	PEEK–carbon fiber 20%	7.97	55.52
	PEEK–carbon fiber 10%	13.6	55.52
	PEEK–glass fiber 40%	14.39	56.17
	PEEK–glass fiber 30%	18.61	56.14
	PEEK–glass fiber 20%	24.32	56.10
	PEEK–glass fiber 10%	35.11	56.02
Rotor 2	Stainless steel	0.94	55.89
	PEEK–carbon fiber 40%	5.2	56.85
	PEEK–carbon fiber 30%	6.99	56.66
	PEEK–carbon fiber 20%	8.95	56.83
	PEEK–carbon fiber 10%	15.27	56.83
	PEEK–glass fiber 40%	11.82	56.89
	PEEK–glass fiber 30%	15.28	56.88
	PEEK–glass fiber 20%	19.98	56.85
	PEEK–glass fiber 10%	28.85	56.84
Rotor 3	Stainless steel	0.97	45.9
	PEEK–carbon fiber 40%	5.31	47.89
	PEEK–carbon fiber 30%	7.15	47.89
	PEEK–carbon fiber 20%	9.15	47.89

Table 11. *Cont.*

Rotor	Material	Maximum Deformation (mm)	Maximum Equivalent Stress (MPa)
Rotor 3	PEEK–carbon fiber 10%	15.61	47.89
	PEEK–glass fiber 40%	12.08	47.89
	PEEK–glass fiber 30%	15.62	47.89
	PEEK–glass fiber 20%	20.42	47.89
	PEEK–glass fiber 10%	29.49	47.89

4. Conclusions

This study successfully developed and optimized a hydrokinetic turbine system capable of adapting to seasonal river velocity variations, significantly improving the CF for energy generation. By designing three interchangeable rotor sizes, the system effectively addressed challenges posed by low winter velocities, maintaining consistent power output across varying flow conditions. Using BladeGen and ANSYS Workbench for rotor design, along with advanced CFD analysis, the turbines achieved a peak efficiency of 43% and 45% by optimizing blade geometry and aerodynamic parameters. The results demonstrated that the rotors consistently produced 5.4 to 5.6 kW of power with a notable increase in the CF by adapting rotor sizes to match seasonal flow variations.

The novelty of this approach lies in several key improvements. First, the analysis shows how to achieve efficiencies of 43% to 45% using CFD. This is achieved through optimization of blade geometry and aerodynamic parameters, ensuring maximum energy capture under varying flow conditions. Second, the system can effectively almost double the CF compared to existing RHKT systems, to which no other approach can compare. This improvement in the CF is critical for enhancing energy production in low-flow conditions, where exciting RHKT systems are underperforming in winter. Additionally, the design features a two-blade rotor, which reduces both costs and complexity during deployment and retrieval. By removing the need for a shroud and gearbox, the system becomes lighter, more reliable, and has fewer components, allowing for easier access and servicing with boats available in remote communities. With three rotors designed, the system allows rotors to be exchanged, depending on the seasonal water velocity. This design is especially beneficial for remote communities, where deployment and maintenance can be managed using local boats, eliminating the need for specialized technicians. The approach is more suited for smaller turbines. Moreover, the structural integrity of the turbine was evaluated using FEA within the Static Structural module of ANSYS Workbench. The analysis demonstrated that PEEK–carbon fiber 40% exhibited minimal displacement and superior performance compared to other materials. The study also validated the simulation results through comparisons with experimental data, confirming the accuracy of the design.

Overall, this research offers a novel and practical solution for improving the performance of river hydrokinetic turbines, particularly for remote communities, by reducing costs, simplifying deployment, and ensuring consistent power generation year-round. The innovative rotor interchangeability concept, combined with material optimization, holds significant promise for advancing renewable energy generation in low-flow environments.

Author Contributions: Conceptualization, B.S.; methodology, B.S.; formal analysis, B.S.; writing original draft preparation, B.S.; writing—review and editing, B.S. and E.L.B.; supervision, E.L.B. and V.C.; project administration, E.L.B.; funding acquisition, E.L.B. All authors have read and agreed to the published version of the manuscript.

Funding: NRCan Clean Energy Fund.

Data Availability Statement: The original contributions presented in the study are included in the article, further inquiries can be directed to the corresponding author.

Acknowledgments: We thank Jinxing Huang for his guidance and Ali Kerrache for his assistance in using the Grex HPC at the University of Manitoba.

Conflicts of Interest: The authors declare no conflicts of interest.

References

1. Doll, P.; Fiedler, K.; Zhang, J. Global-Scale Analysis of River FLow Alterations Due to Water Withdrawals and Reservoirs. *Hydrol. Earth Syst. Sci.* **2009**, *13*, 2413–2432. [CrossRef]
2. Kirke, B. Hydrokinetic and Ultra-Low Head Turbines in Rivers: A Reality Check. *Energy Sustain. Dev.* **2019**, *52*, 1–10. [CrossRef]
3. Kirke, B. Hydrokinetic Turbines for Moderate Sized Rivers. *Energy Sustain. Dev.* **2020**, *58*, 182–195. [CrossRef] [PubMed]
4. Kirke, B. Towards More Cost-Effective River Hydrokinetic Turbines. *Energy Sustain. Dev.* **2024**, *78*, 101370. [CrossRef]
5. Sathyajith, M.; Philip, G.S. (Eds.) *Advances in Wind Energy Conversion Technology*; Environmental Science and Engineering; Springer Berlin Heidelberg: Berlin, Heidelberg, 2011; ISBN 978-3-540-88257-2.
6. Vermaak, H.J.; Kusakana, K.; Koko, S.P. Status of Micro-Hydrokinetic River Technology in Rural Applications: A Review of Literature. *Renew. Sustain. Energy Rev.* **2014**, *29*, 625–633. [CrossRef]
7. Chang, T.-P.; Liu, F.-J.; Ko, H.-H.; Cheng, S.-P.; Sun, L.-C.; Kuo, S.-C. Comparative Analysis on Power Curve Models of Wind Turbine Generator in Estimating Capacity Factor. *Energy* **2014**, *73*, 88–95. [CrossRef]
8. Manwell, J.F.; McGowan, J.G.; Rogers, A.L. *Wind Energy Explained: Theory, Design and Application*, 2nd ed.; John Wiley & Sons Ltd.: Amherst, MA, USA, 2009; ISBN 978-0-470-01500-1.
9. Guney, M.S. Evaluation and Measures to Increase Performance Coefficient of Hydrokinetic Turbines. *Renew. Sustain. Energy Rev.* **2011**, *15*, 3669–3675. [CrossRef]
10. Tan, K.W.; Kirke, B.; Anyi, M. Small-Scale Hydrokinetic Turbines for Remote Community Electrification. *Energy Sustain. Dev.* **2021**, *63*, 41–50. [CrossRef]
11. Muratoglu, A.; Yuce, M.I. Design of a River Hydrokinetic Turbine Using Optimization and CFD Simulations. *J. Energy Eng.* **2017**, *143*, 04017009. [CrossRef]
12. Erwin, S. River Water Surface Velocity Measurement Using Large-Scale Particle Image Velocimetry. Master's Thesis, Department of Mechanical Engineering, University of Manitoba, Winnipeg, MB, Canada, 2023.
13. Gaden, D.L.F.; Bibeau, E.L. A Numerical Investigation into the Effect of Diffusers on the Performance of Hydro Kinetic Turbines Using a Validated Momentum Source Turbine Model. *Renew. Energy* **2010**, *35*, 1152–1158. [CrossRef]
14. Hansen, A.C.; Butterfield, C.P. Aerodynamics of Horizontal Axis Wind Turbines. *Annu. Rev. Fluid Mech.* **1993**, *25*, 115–149. [CrossRef]
15. Md, Q.I.; AKM, S.I. The Aerodynamic Performance of a Horizontal Axis Wind Turbine Calculated by Strip Theory and Cascade Theory. *JSME Int. J.* **1994**, *37*, 871–877.
16. Versteeg, H.K.; Malalasekera, W. *An Introduction to Computational Fluid Dynamics: The Finite Volume Method*, 2nd ed.; Pearson/Prentice Hall: Harlow, UK, 2007; ISBN 978-0-13-127498-3.
17. Duque, E.; Van Dam, C.; Hughes, S. Navier-Stokes Simulations of the NREL Combined Experiment Phase II Rotor. In Proceedings of the 37th Aerospace Sciences Meeting and Exhibit; American Institute of Aeronautics and Astronautics, Reno, NV, USA, 11 January 1999.
18. Serensen, N.N. *Navier-Stokes Predictions of the NREL Phase VI Rotor in the NASA Ames 80-By-120 Wind Tunnel*; Wiley: Hoboken, NJ, USA, 2022.
19. Sarkar, S.; Voke, P.R. Large-Eddy Simulation of Unsteady Surface Pressure Over a Low-Pressure Turbine Blade Due to Interactions of Passing Wakes and Inflexional Boundary Layer. *J. Turbomach.* **2006**, *128*, 221–231. [CrossRef]
20. Franke, J.; Hirsch, C.; Jensen, A.; Krüs, H.; Schatzmann, M.; Westbury, P.; Miles, S.; Wisse, J.; Wright, N. Recommendations on the Use of CFD in Predicting Pedestrian Wind Environment. In Proceedings of the COST Action C14, Impact of Wind and Storm on City Life and the Built Environment, Rhode-Saint-Genèse, Belgium, 5–7 May 2004; pp. C1.1–C1.11.
21. Contreras, L.T.; Lopez, O.D.; Lain, S. Computational Fluid Dynamics Modelling and Simulation of an Inclined Horizontal Axis Hydrokinetic Turbine. *Energies* **2018**, *11*, 3151. [CrossRef]
22. Menter, F.R. Two-Equation Eddy-Viscosity Turbulence Models for Engineering Applications. *AIAA J.* **1994**, *32*, 1598–1605. [CrossRef]

23. Ordonez-Sanchez, S.; Allmark, M.; Porter, K.; Ellis, R.; Lloyd, C.; Santic, I.; O'Doherty, T.; Johnstone, C. Analysis of a Horizontal-Axis Tidal Turbine Performance in the Presence of Regular and Irregular Waves Using Two Control Strategies. *Energies* **2019**, *12*, 367. [CrossRef]
24. Kalkanis, K.; Psomopoulos, C.S.; Kaminaris, S.; Ioannidis, G.; Pachos, P. Wind Turbine Blade Composite Materials—End of Life Treatment Methods. *Energy Procedia* **2019**, *157*, 1136–1143. [CrossRef]
25. Pawar, M.J.; Patnaik, A.; Nagar, R. Mechanical and Thermo-Mechanical Analysis Based Numerical Simulation of Granite Powder Filled Polymer Composites for Wind Turbine Blade. *Fibers Polym.* **2016**, *17*, 1078–1089. [CrossRef]

Disclaimer/Publisher's Note: The statements, opinions and data contained in all publications are solely those of the individual author(s) and contributor(s) and not of MDPI and/or the editor(s). MDPI and/or the editor(s) disclaim responsibility for any injury to people or property resulting from any ideas, methods, instructions or products referred to in the content.